Supporting Information

Lateral CO Diffusion on Micropatterned Ag/CuO Arrays Enables Efficient CO_2-to-C_{2+} Electroreduction

Qi Chen,[a] Yanming Li,[a] Wenbin Ma,[a] Hui Shi,[b] Chunzhen Yang,[a] Changli Li,[a*] Jingfu He[a*]

[a]School of Materials, Shenzhen Campus of Sun Yat-sen University, No. 66, Gongchang Road, Guangming District, Shenzhen, Guangdong 518107, P. R. China

[b]Department of physics, Shanghai Normal University, Shanghai 200234, People's Republic of China

Changli Li* − Email: lichli5@mail.sysu.edu.cn

Jingfu He* − Email: hejf27@mail.sysu.edu.cn

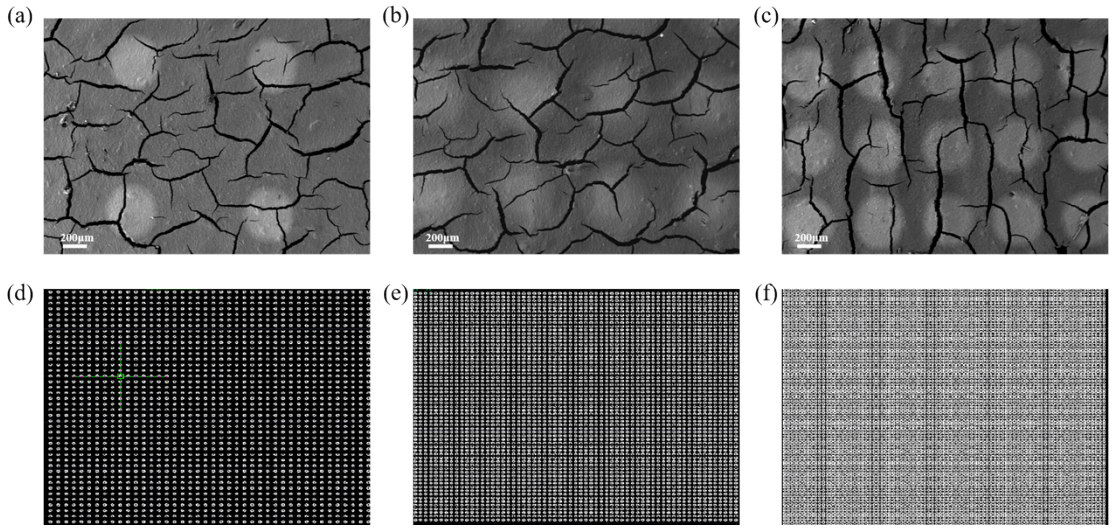

Figure S1. Morphological Characterization of Micropatterned Ag Arrays and Corresponding Mask Designs. (a–c) SEM images of Ag arrays with inter-array spacings of 800 μm, 400 μm, and 200 μm, respectively, demonstrating precise spatial control over the array geometry. (d–f) Schematic diagrams of the corresponding shadow masks used for Ag patterning, highlighting design accuracy and reproducibility.

This figure confirms the precise fabrication of Ag arrays with tunable spacing enabled by tailored mask design.

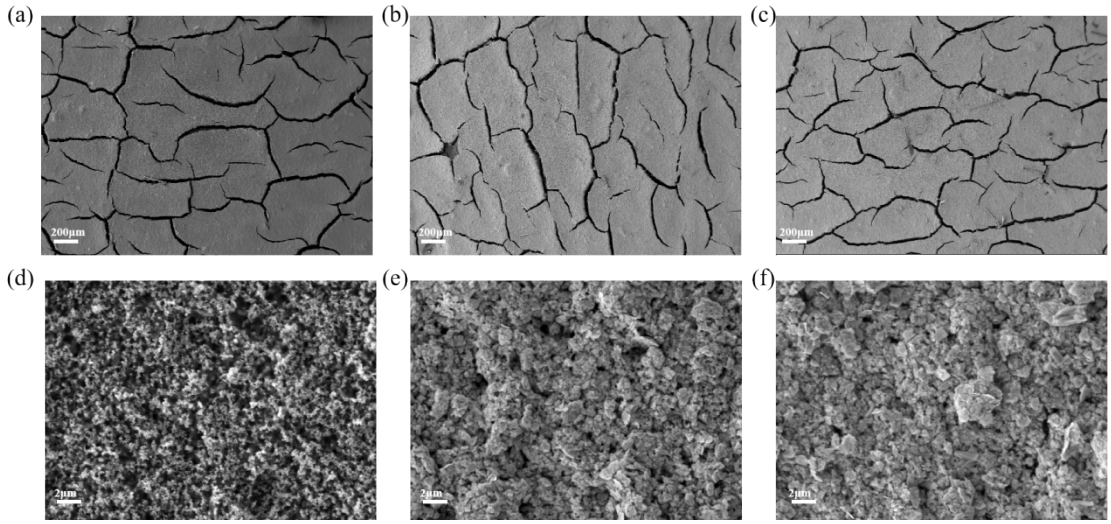

Figure S2. SEM Characterization of Ag, CuO, and Ag–CuO-400 Catalysts. (a–c) SEM images of pure Ag, pure CuO, and Ag–CuO-400 catalysts. (d–f) Higher-magnification SEM images for Ag, CuO and Ag–CuO-400, respectively, revealing surface morphology and the uniform coverage of CuO on the Ag array.

These images demonstrate the morphological distinction among the reference and tandem catalysts, as well as the conformal CuO coating over the Ag arrays.

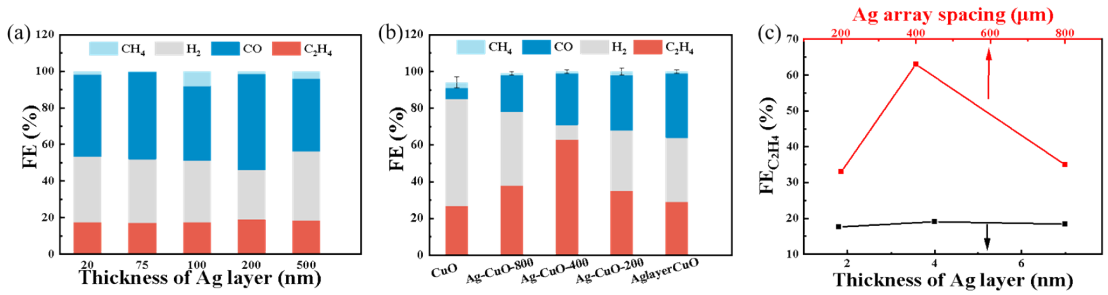

Figure S3. Comparison of Product Selectivity: Vertical Versus Lateral Mass Transport Effects. (a) Gas product distribution as a function of Ag layer thickness (with constant CuO loading), illustrating negligible influence on C_2 product selectivity. (b) Gas product distribution as a function of Ag array spacing (with constant array thickness), showing substantial C_2 product changes and highlighting the dominant role of lateral CO diffusion. (c) Comparison of C_2 selectivity as a function of (lower x-axis) Ag layer thickness with constant spacing, versus (upper x-axis) Ag array spacing with constant thickness; the pronounced difference underscores the prevailing influence of lateral, rather than vertical, transport on tandem catalyst performance.

This figure unambiguously demonstrates that spatial (lateral) arrangement of Ag arrays, rather than vertical stacking or thickness, predominantly governs C_{2+} product selectivity.

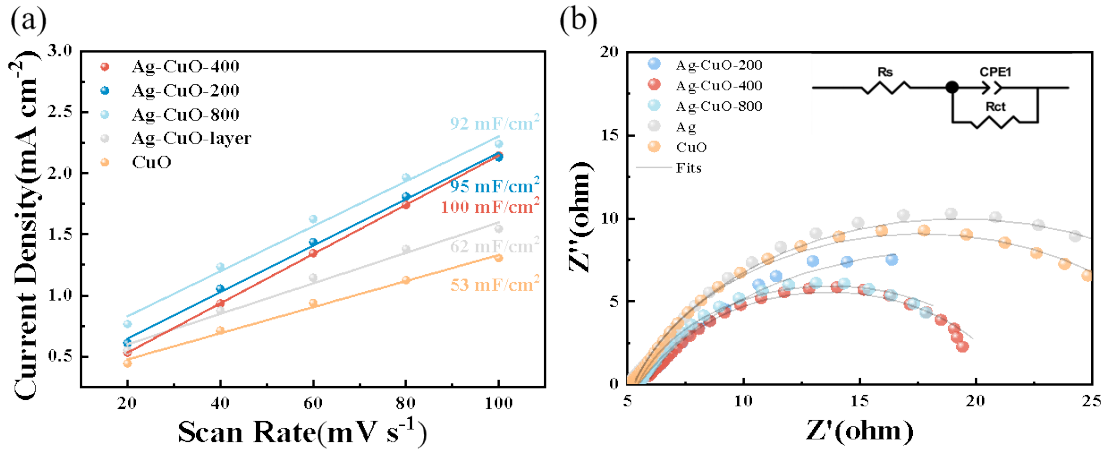

Figure S4. Electrochemical Surface Area and Charge Transfer Properties of Ag Array Catalysts. (a) Electrochemically active surface area (ECSA) evaluated by double-layer capacitance measurements, indicating minimal differences among the Ag array samples. (b) Electrochemical impedance spectroscopy (EIS) Nyquist plots showing comparable charge transfer resistance across all Ag array catalysts.

These results confirm that neither surface area nor intrinsic charge transfer kinetics account for the substantial activity differences among the samples, supporting the conclusion that spatial arrangement is the key determinant of performance.

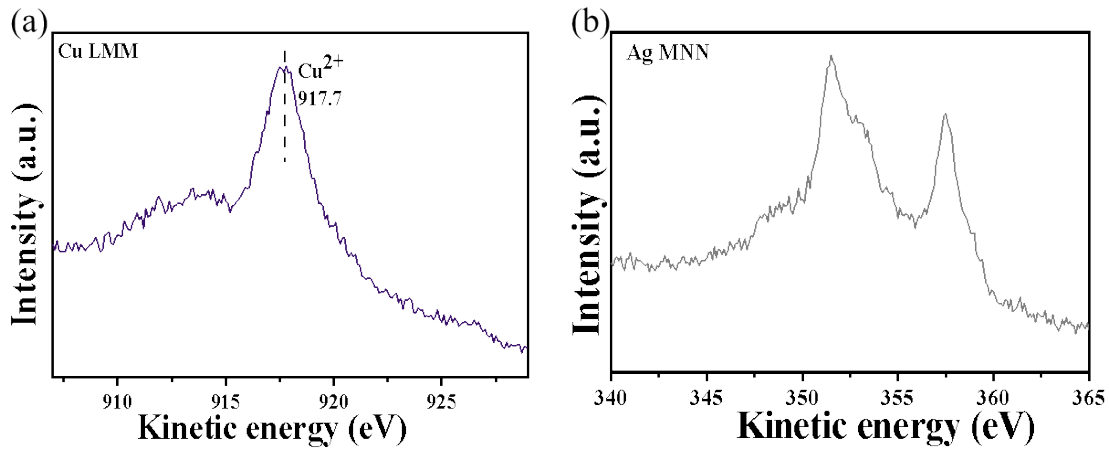

Figure S5. (a) High-resolution Cu LMM Auger kinetic energy spectrum, exhibiting characteristic features consistent with the Cu^{2+} oxidation state in CuO. (b) High-resolution Ag MNN Auger kinetic energy spectrum, confirming the metallic nature (Ag^0) of the Ag arrays.

These results corroborate the XPS analysis, verifying that no significant alloy formation or unexpected oxidation state changes occurred during fabrication.

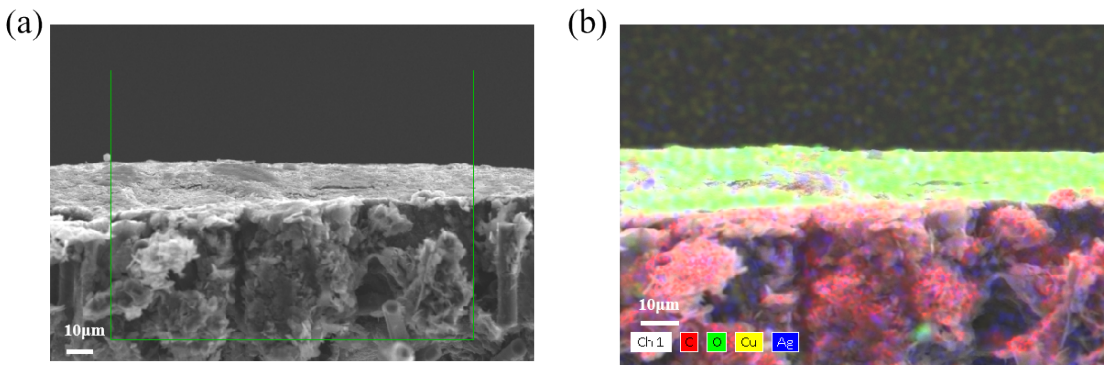

Figure S6. Cross-sectional SEM (a) and EDS (b) characterization of the Ag-CuO-400 electrode.

The image illustrates the interface between the catalytic layer and the gas diffusion layer (GDL). The CuO layer exhibits a dense and uniform morphology covering the carbon fiber substrate.

Note: Due to the significant thickness disparity between the ultra-thin Ag arrays (~20 nm) and the much thicker overlying CuO layer, combined with the roughness of the GDL substrate, the Ag array interface is not visually resolvable in this cross-sectional view. The spatial distribution of Ag arrays is definitively confirmed by the top-down SEM-EDS mapping presented in the main text (Figure 1).

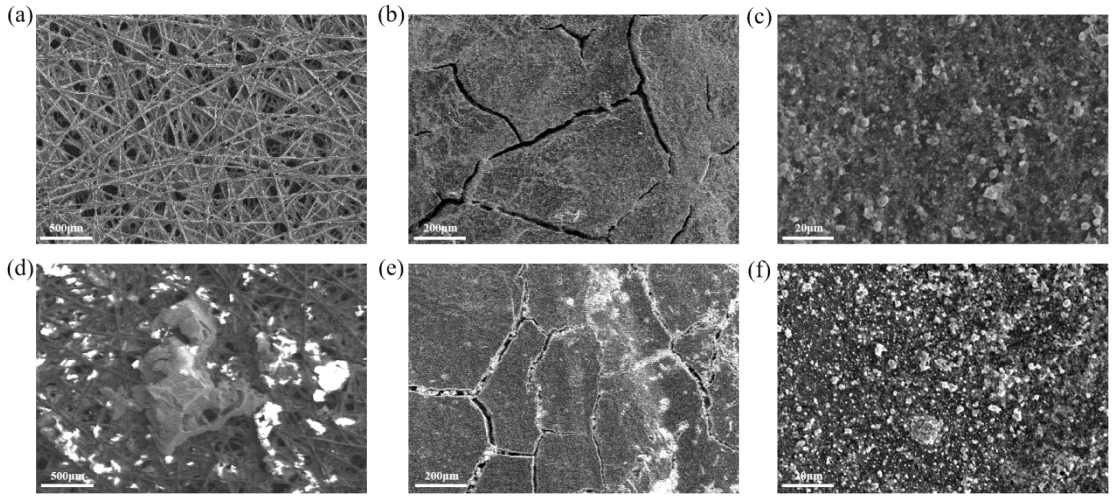

Figure S7. Morphological evolution of the Ag-CuO-400 electrode before and after the long-term stability test. (a-c) SEM images of the fresh electrode: (a) backside of the carbon paper GDL, showing clean carbon fibers; (b, c) top-view of the catalyst layer at different magnifications, displaying well-defined CuO nanoparticles and Ag arrays. (d-f) SEM images of the electrode after 4 hours of continuous electrolysis: (d) backside of the GDL, exhibiting significant accumulation of carbonate crystals; (e, f) top-view of the catalyst layer corresponding to the scales in (b) and (c).

The comparison reveals that the micro/nanostructure of the Ag-CuO catalyst remains intact with no obvious agglomeration or detachment (e-f). In contrast, the GDL backside is heavily clogged by precipitated salts (d), indicating electrolyte penetration and flooding, which impedes gas diffusion and leads to performance decay.

Table S1. Electrochemical impedance spectroscopy (EIS) fitting parameters.

Sample	R_s(Ω)	CPE-T (F cm^{-2})	CPE-P (n)	R_{ct}(Ω)
Ag	5.3	$7.5*10^{-3}$	0.79	27.93
CuO	5.3	$5.4*10^{-3}$	0.80	24.67
Ag-CuO-200	5.2	$8.4*10^{-3}$	0.69	26.45
Ag-CuO-400	5.2	$3.3*10^{-3}$	0.79	15.6
Ag-CuO-800	5.4	$5.3*10^{-3}$	0.79	16.57

The data were fitted using an equivalent circuit of $Rs(QR_{ct})$, where R_s represents the solution resistance, Q(CPE) is the constant phase element representing the double-layer capacitance, and R_{ct} is the charge transfer resistance.

Table S2. Summary of some recently reported Cu-based tandem catalysts for CO_2RR.

Cu-based tandem catalysts		Product	FE (%)	Potential (V *vs.* RHE)	$j_{partial}$/ ($mA \cdot cm^{-2}$)	Electrolytic cell	Stability (h)	Electrolyte	Ref.
Metallic alloys	Cu_4Zn	C_2H_5OH	29.1	-10.5	-8.2	H-cell	5	0.1 M $KHCO_3$	[1]
	$Cu_{500}Ag_{1000}$	C_{2+}	\	-0.7	-160	Flow cell	2	1 M KOH	[2]
	Ag/Cu	C_2H_4	42	-1.1	-2.31	H-cell	30	0.1 M $KHCO_3$	[3]
	$Cu_{1.0}/ZnO_{0.2}$	C_2H_4	49	-0.73	-292	Flow cell	10	1 M KOH	[4]
Metallic heterojunction	Cu_{oh}-Ag	C_2H_5OH	23.1	-1.4	2.5	H-cell	\	0.1 M $KHCO_3$	[5]
	Ag_{65}-Cu_{35}	C_2H_4	54	-1.2	-2	H-cell	10	0.1 M $KHCO_3$	[6]
Metallic core-shell structures	Cu@Ag-2	C_2H_4	32.2	-1.1	-9	Flow cell	14	1 M KOH	[7]
	Au@Cu_2O yolk-shell	C_2H_5OH	52.3	−0.3	\	H-cell	\	0.1 M $KHCO_3$	[8]
Cu-based carbon materials	Cu/N-CNF	C_2H_4	62	-0.57	-373	Flow cell	10	5 M KOH	[9]
Cu-Based polymer modified materials	Cu0@PIL @CuI	C_{2+}	76.1	-0.85	-304.2	Flow cell	40	1 M KOH	[10]
Ag array-CuO	**Ag-CuO-400**	**C_2H_4**	**63**	**-2**	**-300**	**Flow cell**	**4**	**0.5M $KHCO_3$**	**Our work**

1 D. Ren, B. S.-H. Ang and B. S. Yeo, *ACS Catal.*, 2016, **6**, 8239–8247.
2 C. Chen, .
3 J. Wang, Z. Li, C. Dong, Y. Feng, J. Yang, H. Liu and X. Du, *ACS Appl. Mater. Interfaces*, 2019, **11**, 2763–2767.
4 T. Zhang, Z. Li, J. Zhang and J. Wu, *J. Catal.*, 2020, **387**, 163–169.
5 P. Iyengar, M. J. Kolb, J. R. Pankhurst, F. Calle-Vallejo and R. Buonsanti, *ACS Catal.*, 2021, **11**, 4456–4463.
6 Y. Ma, J. Yu, M. Sun, B. Chen, X. Zhou, C. Ye, Z. Guan, W. Guo, G. Wang, S. Lu, D. Xia, Y. Wang, Z. He, L. Zheng, Q. Yun, L. Wang, J. Zhou, P. Lu, J. Yin, Y. Zhao, Z. Luo, L. Zhai, L. Liao, Z. Zhu, R. Ye, Y. Chen, Y. Lu, S. Xi, B. Huang, C. Lee and Z. Fan, *Adv. Mater.*, 2022, **34**, 2110607.
7 S. Zhang, S. Zhao, D. Qu, X. Liu, Y. Wu, Y. Chen and W. Huang, *Small*, 2021, **17**, 2102293.
8 B.-B. Zhang, Y.-H. Wang, S.-M. Xu, K. Chen, Y.-G. Yang and Q.-H. Kong, *RSC Adv.*, 2020, **10**, 19192–19198.
9 J.-C. Lee, J.-Y. Kim, W.-H. Joo, D. Hong, S.-H. Oh, B. Kim, G.-D. Lee, M. Kim, J. Oh and Y.-C. Joo, *J. Mater. Chem.a*, 2020, **8**, 11632–11641.
10 G. Duan, X. Li, G. Ding, L. Han, B. Xu and S. Zhang, *Angew. Chem. Int. Ed.*, 2022, **61**, e202110657.